

Influence of Flux Barriers and Permanent Magnet Arrangements on Performance of High-Speed Flux-Intensifying IPM Motor

Thanh-Anh Huynh¹, *Member, IEEE*, Yen-Truc Nguyen Le¹, Zhen Lee^{1,2}, Mi-Ching Tsai², *Fellow, IEEE*, Po-Wei Huang², and Min-Fu Hsieh^{1,*}, *Senior Member, IEEE*

¹Department of Electrical Engineering, National Cheng Kung University, Tainan 701, Taiwan

²Electrical Motor Technology Research Center, National Cheng Kung University, Tainan 701, Taiwan

This paper investigates the effects of multiple flux barriers (FBs) and permanent magnet (PM) arrangements of flux intensifying (FI) interior PM (FI-IPM) motors at high-speed operation for spindle applications. Common FI-IPM motors possess a low constant power speed range (CPSR), thus limiting their applications. In this paper, three multiple-flux-barrier FI-IPM (MFI-IPM) motors with different PM arrangements are studied. First, the air gap flux density, inductance characteristics, and torque component distribution are investigated with various rotor topologies. Then, the performance of the MFI-IPM motors in terms of CPSR and torque ripple is investigated and compared with an original V-shape FI-IPM motor. The analysis reveals that proper rotor designs can significantly improve the performance and CPSR of the MFI-IPM motor. Furthermore, considering the rotor mechanical strength of the MFI-IPM motor at high speeds, magnetic bridges and ribs are added, which thus increases flux leakage and slightly reduces motor performance. Finally, a rated power of 9 kW MFI-IPM motor prototype is fabricated and tested. The experiment results validate the analyses.

Index Terms— Flux Intensifying, Interior Permanent Magnet Motors, Multiple Flux Barriers, Industry.

I. INTRODUCTION

INTEREST in high-speed machine development has surged in recent years for applications like spindle motors, which require precision and superior surface finish in machining [1]. While conventional induction motors are the most popular candidate, permanent magnet synchronous motors (PMSMs) have gained attention for spindle applications due to their high-power density, efficiency, dynamic response, and direct coupling to mechanical loads [2]. To extend the motor speed range, the magnetic field of PMSMs is weakened using a d -axis current (i_d). However, this poses demagnetization risks and impacts motor performance [3, 4].

To overcome the demagnetization problem, the flux-intensifying interior permanent magnet (FI-IPM) motor was introduced [5]. This motor leverages flux-intensifying (FI) current at low speeds to generate both reluctance and electromagnetic torque, minimizing the need for deep flux-weakening (FW) at high speeds, leading to an improved motor performance with reduced demagnetization risks. Consequently, thinner magnets can be used in the FI-IPM motor design, which offers cost advantages compared to conventional PMSMs [6].

On the other hand, constant power speed range (CPSR) is a critical performance metric for motors in specific applications. Enhancing the motor's FW capability is key to achieving a wider CPSR, necessitating a designed characteristic current (I_{ch}) close to the armature current (I_s). However, conventional FI-IPM (CFI-IPM) motors are often designed with a saliency ratio (L_d/L_q) close to 1, resulting in low reluctance torque and reducing the FW ability due to strong PM flux linkage [5, 6, 7]. Thus, increasing the d -axis inductance or reducing the PM flux linkage is necessary to boost reluctance torque and enhance the FW capability [8]. This can be done by incorporating additional flux barriers or manipulating PM arrangements in the rotor. Multiple flux barriers have been explored for FI-IPM motors

and reported in [5, 9, 10]; however, they exhibit limited CPSR and often suffer weak rotor structural strength for high-speed operation. Meanwhile, segmented PMs have demonstrated higher CPSR values (≥ 3) for FI-IPM motors [11, 12]. Thus, it can be observed that combining multiple flux barriers and PM arrangements to improve flux weakening ability, enhance motor performance, and extend CPSR merits further investigation.

This paper studies the combined impact of multiple flux barriers and PM arrangements on the performance and CPSR of FI-IPM motors with I-shaped PM. Three multiple-flux-barrier FI-IPM (MFI-IPM) models are developed and compared to the CFI-IPM model with V-shape PM. The paper outlines the design principles and rotor development of the MFI-IPM models based on the CFI-IPM motor. The influence of flux barrier widths on motor torque is examined, followed by an evaluation and comparison of air gap flux density, inductances, and torque. The study also analyzes motor performance in terms of torque ripple and CPSR, along with assessing the structural strength of these motors at high speeds. Finally, the designs are validated through finite element analysis (FEA) and experiments.

II. RESEARCH METHOD AND TARGET MODELS

A. Background

The FW ability and CPSR of motors can be improved by manipulating the PM flux linkage and d -axis inductance. Thus, to maximize the FW capability, the condition should be met.

$$I_s = I_{ch} = \lambda_{pm}/L_d \quad (1)$$

where I_s and I_{ch} are the armature and characteristic current, respectively; λ_{pm} is PM flux linkage, and L_d is d -axis inductance.

The characteristics of the FI-IPM motors can be given as [5-7]

$$(i_d + \lambda_{pm}/L_d)^2 / (V_s/\omega_e L_d)^2 + i_q^2 / (V_s/\omega_e L_q)^2 = 1 \quad (2)$$

where i_d and i_q are d - q axis current, L_q is q -axis inductance, ω_e is electrical speed, and V_s is the voltage limit of the inverter.

TABLE I
SPECIFICATIONS AND PARAMETERS OF FI-IPM MOTORS

Item	Unit (Value)
Stator Outer/Inner Diameters	182.5 mm / 117.7 mm
Rotor Outer/Inner Diameters	116.7 mm / 29 mm
Air gap length	0.5 mm
Number of slots/poles	36/ 6
Peak/Rated torque	28 Nm / 16 Nm
Peak/Rated current	55A/ 30A
Maximum speed	12000 rpm
Peak/Rated power	15 kW/ 9 kW
Limit voltage	380V
Stator/Rotor materials	35CS250
PM material	N38UH

B. Studied Models and Design Evolution of Rotor Topology

In this study, a benchmark 36-slot/6-pole 15 kW CFI-IPM motor is designed using a V-shape magnet configuration (based on [7]), as shown in Fig. 1(a). Based on this motor, three FI-IPM models with multiple flux barriers and an I-shape magnet are developed, denoted "MFI-IPM1", "MFI-IPM2", and "MFI-IPM3", as indicated in Fig.1 (b), (c), and (d). Note that the CFI-IPM motor was designed with a high magnetic flux density, thus I_{ch} being nearly twice I_s . To maximize the FW capability and CPSR, the evolution of the rotor topology for MFI-IPM motors should satisfy the condition given in (1), which includes the designs of PMs and flux barriers, as shown in Fig. 1.

The design concept for the rotor of the MFI-IPM motors is as follows. First, to reduce the flux density, the V-shaped magnet is replaced with an I-shaped one. Modifications are then made to the outer flux barrier, and some flux barriers are added on the q -axis of the CFI-IPM motor, increasing the inductance on the d -axis (L_d). Consequently, the CFI-IPM motor is transformed into the MFI-IPM1 motor, as depicted in Fig. 1(b).

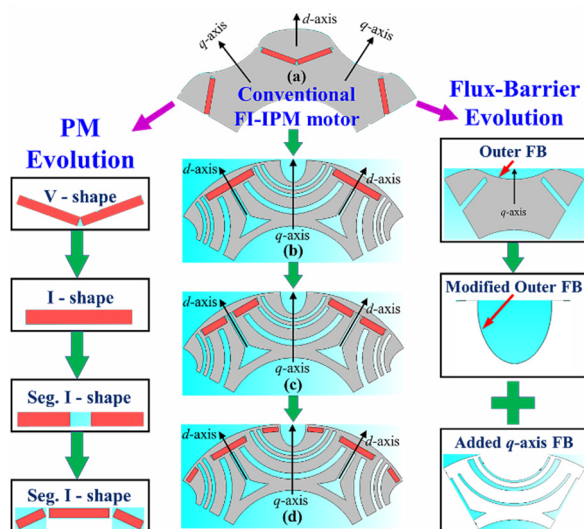


Fig. 1. 15 kW FI-IPM motors and rotor design evolution from conventional FI-IPM motor to the multiple-flux-barrier FI-IPM motors. (a) CFI-IPM, (b) MFI-IPM1, (c) MFI-IPM2, (d) proposed MFI-IPM3 model.

Next, to minimize the I_{ch} , the I-shaped magnet is segmented for MFI-IPM2 (2-seg.) and MFI-IPM3 (3-seg.), as indicated in Figs. 1(c) and (d), respectively. Note that the position of the magnets to the outer edge of the rotor for the MFI-IPM models remains the same, and the width of the added flux barriers on the torque of MFI-IPM motors should be sufficient to achieve

maximum torque. To ensure a fair comparison, all the models are designed with a peak power of 15 kW and the same number of slots/poles, dimensions, PM volume, winding layouts, and voltage. The base speed of each model may slightly differ to achieve the same power. The specifications and parameters of these motors are given in Table I.

III. Q-AXIS ADDED FLUX BARRIERS ON MFI-IPM TORQUE

To enhance L_d of the MFI-IPM motors, flux barriers are strategically placed along the q -axis. However, the widths of these flux barriers directly impact the motor torque. Therefore, careful investigation is needed. To address this issue, three specific flux barriers: FB1, FB2, and FB3 are evaluated and illustrated in Fig. 2.

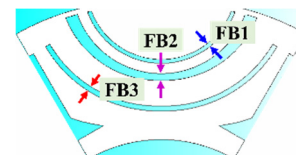


Fig. 2. Investigation of flux-barrier design parameters for MFI-IPM motors.

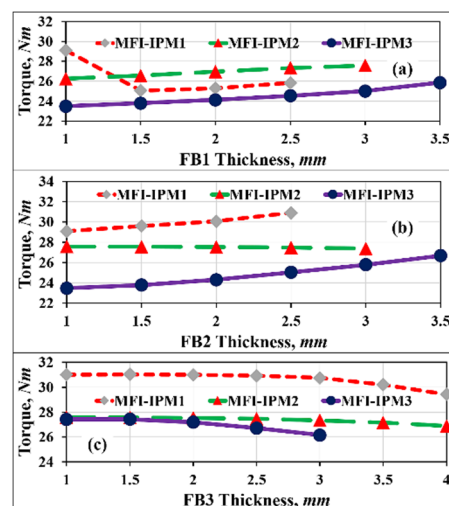


Fig. 3. Investigation of flux-barrier design parameters for MFI-IPM motors.

Fig. 3 compares the effect of the three flux barrier designs on the torque of the MFI-IPM motors. Note that the widths of the flux barriers differ in each MFI-IPM, which considers their positions and space in the rotor core. As can be seen in Fig. 3, the torque of the MFI-IPM1 motor decreases with increasing FB1, while that of the other two increases. Similarly, the torque of MFI-IPM1 and MFI-IPM3 increases with increasing FB2, and that of MFI-IPM2 remains constant. Conversely, a slight reduction in torque is observed for all the MFI-IPM motors when FB3 increases. Hence, the widths of the designed flux barriers should be carefully determined to achieve maximum torque, as summarized in Table II.

TABLE II
COMPARISON OF WIDTH OF FLUX BARRIERS TO ACHIEVE MAXIMUM TORQUE FOR EACH MFI-IPM MOTOR

Items	MFI-IPM1	MFI-IPM2	MFI-IPM3
FB1 (mm)	1	3	1.5
FB2 (mm)	2.5	1	3.5
FB3 (mm)	1	1	1.5
Torque (Nm)	30.92	27.58	27.4

IV. MOTOR PERFORMANCES ANALYSIS AND COMPARISON

Upon finalizing the rotor design parameters for the MFI-IPM motors, comprehensive performance analysis and comparison with the CFI-IPM motor are conducted. The analysis will shed light on the performance characteristics and highlight any notable differences between the MFI-IPM and CFI-IPM motors.

A. Air Gap Flux Density and Back EMF Comparisons

Fig. 4 provides a comparison of air gap flux density between the three MFI-IPM models and the CFI-IPM model in one mechanical rotational cycle. As can be seen, MFI-IPM1, featuring multiple flux barriers, shows a slight decrease in air gap flux density compared to the CFI-IPM model. Furthermore, a significant reduction in air gap flux density is observed for the MFI-IPM2 and MFI-IPM3 models, where the PM is segmented.

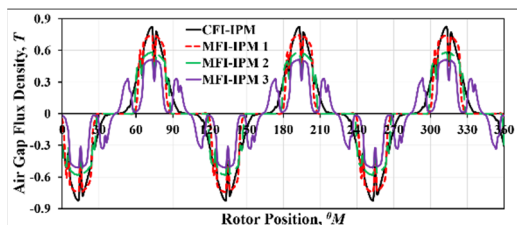


Fig. 4. Comparison of air-gap flux density distributions between different FI-IPM models.

Fig. 5 compares the back EMF waveforms of all the models at 6000 rpm. It can be seen that the waveform of CFI-IPM is nearly sinusoidal. However, the presence of flux barriers and the arrangement of PMs result in a reduction in the amplitude of the back EMF for the MFI-IPM models, especially MFI-IPM3. However, this enhances the reluctance torque due to the increased saliency compared to other models. Fig. 6 shows that the total harmonic distortion (THD) of the back EMF in the MFI-IPM models increases considerably compared to the CFI-IPM model. As a result, the torque ripple of the MFI-IPM models would be higher than that of the CFI-IPM model.

B. Inductance and Torque

Fig. 7 presents a detailed analysis of inductance features for the MFI-IPM and CFI-IPM models. It can be observed that the flux barriers cause the d -axis inductance of MFI-IPM1 to increase, while the q -axis inductance remains the same compared to CFI-IPM, as shown in Fig. 7(a) and (b). This leads to an increase in the saliency ratio (L_d/L_q) in MFI-IPM1. However, when a single PM layer is divided into two pieces, the q -axis inductance decreases significantly, resulting in a significant reduction in the saliency ratio, as shown in Fig. 7(c).

To enhance the flux-intensifying effect, the design of flux barriers and PM arrangement is modified, as depicted in Fig. 1(d). This modification leads to a substantial increase in the d -axis inductance of the MFI-IPM3 model while maintaining the q -axis inductance compared to CFI-IPM and MFI-IPM1. Consequently, the saliency ratio of MFI-IPM3 is significantly boosted and becomes the highest among these models.

Fig. 8 compares the torque components distribution between the MFI-IPM and CFI-IPM models at peak armature current. The CFI-IPM model exhibits the highest total torque (32.5 Nm) and high reluctance torque. However, the presence of flux

barriers in the MFI-IPM1 model results in a slight reduction in both total torque and reluctance torque. Meanwhile, in MFI-IPM2 (PM with two segments), the total torque significantly decreases (27.58 Nm) due to the reduction of PM torque, while the reluctance torque remains relatively unchanged. Conversely, modifying the PM arrangement in the MFI-IPM3 model leads to a significant increase in reluctance torque, despite the decrease in total torque. This enhancement in reluctance torque of MFI-IPM3 improves the CPSR.

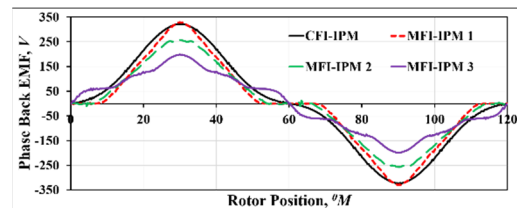


Fig. 5. Comparison of Back EMF between different FI-IPM models. (a) CFI-IPM, (b) MFI-IPM1, (c) MFI-IPM2, (d) MFI-IPM3.

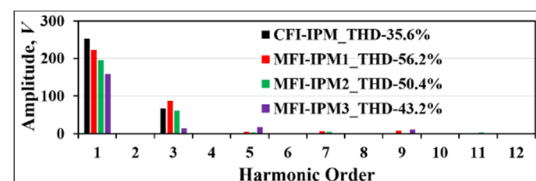


Fig. 6. Comparison of Back EMF harmonics between FI-IPM models.

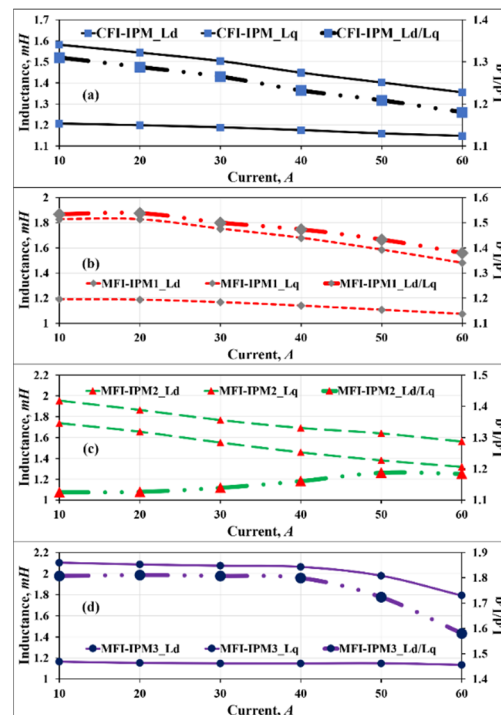


Fig. 7. Inductance features variation with the armature current of the different FI-IPM machines. (a) CFI-IPM, (b) MFI-IPM1, (c) MFI-IPM2, (d) MFI-IPM3.

C. Torque and Performance of Motors in Wide Speed Range

Fig. 9(a) shows the steady torque of the MFI-IPM and CFI-IPM models at a load current of 55 A. The CFI-IPM model exhibits an average torque of 32.5 Nm with a torque ripple of around 4% at a current phase advance of -5° E. The average torque for MFI-IPM1, MFI-IPM2, and MFI-IPM3 is 30.92 Nm, 27.58 Nm, and 27.4 Nm, at current phase advances of -10° E for MFI-IPM1, MFI-IPM2 and -20° E for MFI-IPM3, respectively.

The torque ripple for MFI-IPM2, MFI-IPM1, and MFI-IPM3 is 5%, 6%, and 9.6%, respectively. It can be observed that the average torque of the MFI-IPM models significantly reduces, especially for MFI-IPM3, due to the effect of flux barriers and PM arrangement compared to that of CFI-IPM.

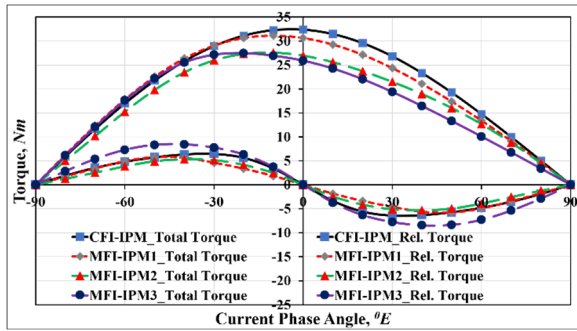


Fig. 8. Comparison of torque distributions between different FI-IPM models.

Fig. 9(b) shows that the maximum total torque of the MFI-IPM and CFI-IPM motors is achieved with a positive i_d , indicating that $L_d > L_q$ (Fig. 7). When a positive i_d is applied, a positive reluctance torque is achieved (Fig. 8). With the highest positive reluctance torque, MFI-IPM3 demonstrates that the rotor design enhances the flux-intensifying effect.

Fig. 10 shows the torque-speed and power-speed curves of the four motors. Although the PM flux linkage of the MFI-IPM models is lower than that of the CFI-IPM model (Fig. 4), MFI-IPM1 and MFI-IPM2 achieve the same CPSR ($=3$) as CFI-IPM. This is because I_{ch} of these three models lies outside the circle of the current limit I_s . Thus, the CPSR of the CFI-IPM, MFI-IPM1, and MFI-IPM2 models is restricted. Meanwhile, MFI-IPM3, which features properly arranged flux barriers and PMs, has a relatively larger reluctance torque owing to its relatively larger L_d and smaller PM flux density than other models. This makes I_{ch} of MFI-IPM3 lies inside the circle of armature current limit, thereby enhancing its flux-weakening ability. As a result, MFI-IPM3 exhibits a significant increase in the maximum operating speed and a CPSR extension to more than 5. Thus, the MFI-IPM3 design offers a wide speed range with a high CPSR. The comparison of I_{ch} and I_s between the MFI-IPM motors and the CFI-IPM motor is illustrated in Table III.

V. MECHANICAL STRENGTH OF MFI-IPM

Using multiple flux barriers in the rotor presents a significant challenge to mechanical strength, particularly at high speeds. Hence, a mechanical stress analysis is carried out to evaluate the robustness of the rotor core. The structural analysis in this study was conducted without considering the adhesive properties between the rotor core and PMs. Note that the magnetic force is neglected as the centrifugal force is deemed to be dominant, especially at high speeds [12].

TABLE III
COMPARISON OF I_{ch} AND I_s BETWEEN FOUR FI-IPM MODELS

Items	CFI-IPM	MFI-IPM1	MFI-IPM2	MFI-IPM3
λ_{pm} (Wb)	0.134	0.1186	0.1058	0.0852
L_d (mH)	1.356	1.481	1.562	1.792
I_{ch} (A)	98.84	80.1	67.71	47.52
I_s (A)	55	55	55	55

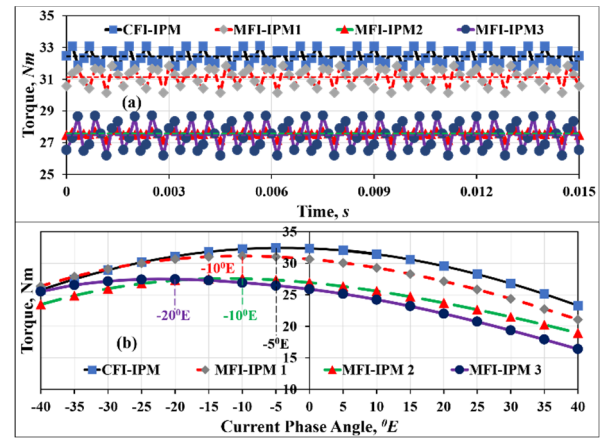


Fig. 9. Torque distributions between different FI-IPM models. (a) Steady torque. (b) Torque varies with the current angle.

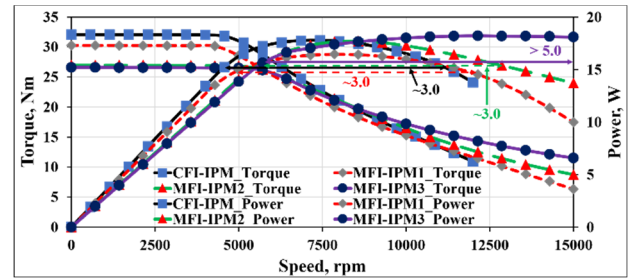


Fig. 10. The torque-speed and power-speed curves of the four FI-IPM machines. The CPSR of CFI-IPM, MFI-IPM1, and MFI-IPM2 = 3 and MFI-IPM3 > 5.

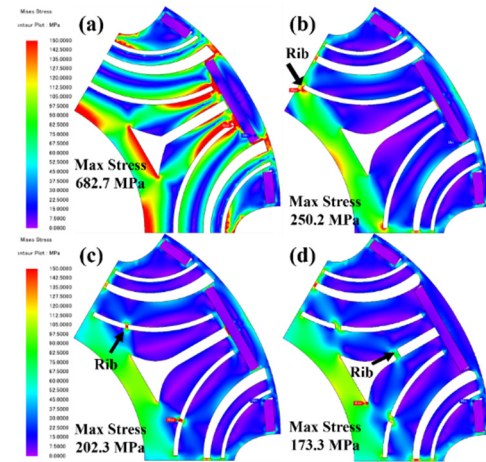


Fig. 11. von Mises stress of MFI-IPM3 at 12000 rpm with/without ribs design.

Fig. 11 shows the distribution of the von Mises stresses in the rotor of MFI-IPM3 at 12,000 rpm. The electric steels (35CS250, provided by China Steel Corp., Taiwan) possess yield stress of 400 MPa. However, the maximum von Mises stress of MFI-IPM3 is 682.7 MPa, indicating an insufficient mechanical strength, as shown in Fig. 11(a). To improve this, reinforcement ribs are added to the rotor core, as shown in Fig. 11(b). This results in a distribution of the maximum von Mises stress of the MFI-IPM3 model reducing to 250.2 MPa. To achieve a safety factor greater than 2, more ribs are further inserted to enhance the strength, as shown in Figs. 11(c) and (d). As a result, the maximum von Mises stress of MFI-IPM3 is reduced to 173 MPa, which meets the strength required.

The introduction of reinforcement ribs in the rotor core impacts the torque and torque ripple of MFI-IPM3, as given in

Table IV. The torque value decreases from 27.4 Nm to 26.7 Nm, while the torque ripple slightly increases from 9.6% to 11.3%.

TABLE IV
EFFECT OF REINFORCEMENT RIBS ON TORQUE AND TORQUE RIPPLE OF MFI-IPM3 MODEL

Without reinforcement ribs	Unit (Value)
Torque / Torque Ripple	27.4 Nm / 9.6 %
With reinforcement ribs	Unit (Value)
Torque / Torque Ripple	26.7 Nm / 11.3 %

VI. EXPERIMENT

Finally, based on MFI-IPM3, a prototype was fabricated for experimental validation, as depicted in Fig. 12. To evaluate the performance of the prototype, a series of tests were conducted. The first step involved measuring the motor under no-load conditions, as shown in Figs. 13 and 14. The back EMFs at 1000 rpm were compared between the simulation and measurement, and the phase back-EMF peak values were 22.9 V and 20.8 V, respectively, with an acceptable error of 9.5%. This error could be attributed to unexpected leakage flux in the prototype. Nevertheless, the simulation is validated.

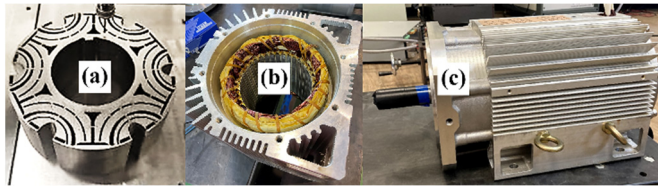


Fig. 12. The prototype of the MFI-IPM3 model. (a) rotor core, (b) stator core, (c) prototype after assembly.

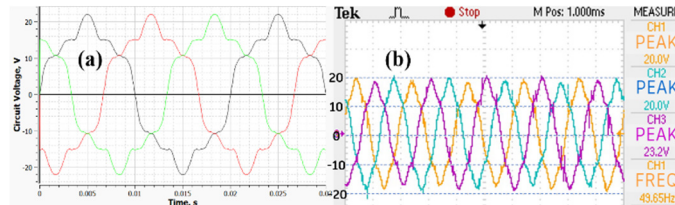


Fig. 13. Back EMFs: (a) simulation; (b) experiment @ 1000 rpm.

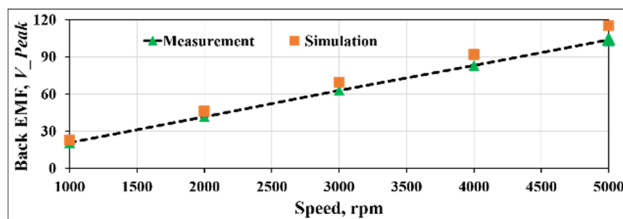


Fig. 14. Comparison of back EMFs.

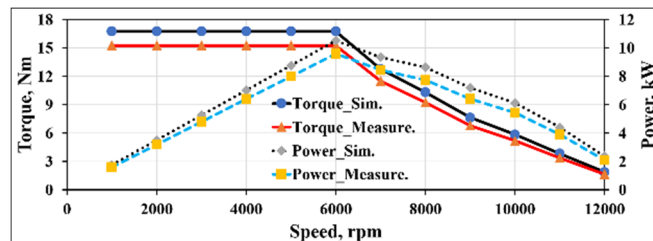


Fig. 15. Comparison of torque and power versus speed curves by experiments.

Then, the prototype was tested at rated conditions, and the measured output torque and power were compared with the simulations, as presented in Fig. 15. The simulation predicted

an output torque of 16.75 Nm, which is maintained till the motor base speed of 6000 rpm under the voltage limit, and an output power of 10.5 kW. In contrast, the test recorded an output torque of 15.3 Nm and power of 9.6 kW in the same operational condition. The difference between the two cases may also be caused by the leakage flux in the prototype. The experiment can still sufficiently validate the simulation and analysis.

VII. CONCLUSION

This paper has studied the effect of multiple flux barriers and PM arrangements of FI-IPM motors on CPSR, torque, and mechanical strength at high speed. Three MFI-IPM models using a single PM layer were developed to compare with the CFI-IPM one using V-shape magnets. The results revealed that, with a proper rotor design, the MFI-IPM3 model could achieve an excellent CPSR (>5); however, the structural strength needs to be carefully considered. Finally, the prototype was tested, and the experiments validated the analysis.

ACKNOWLEDGMENT

JSOL Corporation is acknowledged for supporting JMAG.

REFERENCES

- [1] A. Tenconi, S. Vaschetto, and A. Vigliani, "Electrical Machines for High-Speed Applications: Design Considerations and Tradeoffs," *IEEE Trans. Ind. Electron.*, vol. 61, no. 6, pp. 3022-3029, June 2014.
- [2] M. T. B. Tarek, and S. Choi, "Design and rotor shape modification of a multiphase high speed permanent magnet assisted synchronous reluctance motor for stress reduction," in *Proceeding of IEEE Energy Conversion Congress and Exposition (ECCE)*, October 2017, USA.
- [3] T. A. Huynh, J.-X. Peng, M.-F. Hsieh, P.-W. Huang, "Anti-Demagnetization Analysis of Fractional Slot Concentrated Windings Interior Permanent Magnet Motor Considering Effect of Rotor Design Parameters," *IEEE Trans. Magn.*, vol. 58, no. 2, pp. 1-6, February 2022.
- [4] T. A. Huynh, M.-F. Hsieh, "Irreversible Demagnetization Analysis for Multilayer Magnets of Permanent Magnet-Assisted Synchronous Reluctance Machines Considering Current Phase Angle," *IEEE Trans. Magn.*, vol. 55, no. 7, pp. 1-9, July 2019.
- [5] N. Limsuwan, Y. Shibukawa, D. D. Reigosa, and R. D. Lorenz, "Novel Design of Flux-Intensifying Interior Permanent Magnet Synchronous Machine Suitable for Self-Sensing Control at Very Low Speed and Power Conversion," *IEEE Trans. Ind. Appl.*, vol. 47, no. 5, pp. 2004-2012, 2011.
- [6] D.-K. Ngo, M.-F. Hsieh, T. A. Huynh, "Torque Enhancement for a Novel Flux Intensifying PMA-SynRM Using Surface-Inset Permanent Magnet," *IEEE Trans. Magn.*, vol. 55, no. 7, pp. 1-8, June 2019.
- [7] T. Wang, X. Zhu, S. Zheng, L. Quan, Z. Xiang, and X. Zhou, "Investigation on Torque Characteristic and PM Operation Point of Flux-Intensifying PM Motor Considering Low-Speed Operation," *IEEE Trans. Magn.*, vol. 57, no. 2, pp. 1-5, 2021.
- [8] T. A. Huynh, M.-F. Hsieh, "Comparative Study of PM-Assisted SynRM and IPMSM on Constant Power Speed Range for EV Applications," *IEEE Trans. Magn.*, vol. 53, no. 11, pp. 1-6, November 2017.
- [9] F. Liu, X. Zhu, W. Wu, L. Quan, Z. Xiang, and Y. Hua, "Design and Analysis of an Interior Permanent Magnet Synchronous Machine with Multiflux-Barriers Based on Flux-Intensifying Effect," *IEEE Trans. Appl. Supercond.*, vol. 28, no. 3, April 2018.
- [10] M. Kashif, B. Singh, "Design optimization with improved torque performance of a new flux-intensifying PMSM using multilayer barriers for solar water pumps," *Eng. Sci. Technol., Inter. J.*, vol. 36, 101134, 2022.
- [11] X. Zhu, S. Yang, Y. Du, Z. Xiang, and L. Xu, "Electromagnetic Performance Analysis and Verification of a New Flux-Intensifying Permanent Magnet Brushless Motor With Two-Layer Segmented Permanent Magnets," *IEEE Trans. Magn.*, vol. 52, no. 7, pp. 1-4, 2016.
- [12] X. Zhu, W. Wu, S. Yang, Z. Xiang, and L. Quan, "Comparative Design and Analysis of New Type of Flux-Intensifying Interior Permanent Magnet Motors With Different Q-Axis Rotor Flux Barriers," *IEEE Trans. Energy. Conver.*, vol. 33, no. 4, pp. 2260-2269, 2018.